JOURNAL OF PROPULSION AND POWER
Vol. 26, No. 5, September–October 2010

Magnetic Ion Beam Deflection in the Helicon Double-Layer Thruster

Wes Cox,* Christine Charles,† and Rod W. Boswell‡
Australian National University, Acton 0200, Australia
and
Robert Laine§ and Matthew Perren¶
ASTRIUM-EADS, 75016 Paris, France

DOI: 10.2514/1.49202

Transverse magnetic fields (along the *x*-axis, transverse to the *z*-axis) are applied to a helicon double-layer plasma to investigate the effect on the ion beam accelerated in the electric field of the double-layer. The 250 W radio frequency argon plasma is operated at a pressure of 0.04 Pa in a diverging magnetic field with a maximum of ∼140 G along the primary axis (*z*-axis). The diverging magnetic field is produced by two primary solenoids aligned coaxially along the *z*-axis. Introducing an additional solenoid mounted along the *x*-axis, perpendicular to the *z*-axis, generates a 0 to 250 G magnetic field at its center (0 to 55 G at the *z*-axis) as the supplied current is swept from 0 to 6 A. Spatial measurements of the ion beam downstream of the double-layer using a retarding field energy analyzer reveal deflection of the ion beam vector, with the angle of deflection increasing with increasing transverse solenoidal current. Deflection of the ion beam is observed for both transverse solenoidal polarities, with the polarity determining the direction of ion beam deflection. Under the influence of the transverse magnetic field, the ion beam vector is demonstrated to be deflected in the *x*-*z* plane as a function of the transverse solenoidal polarity. The ion beam is measured to be deflected by up to −26 and 14 deg for the transverse polarity pointing out of and into the thruster, respectively, where positive deflection is defined in the positive *x*-direction.

Nomenclature

$\|B\|$	=	magnetic field magnitude, G
B_x	=	*X*-component of the magnetic field, G
B_z	=	*Z*-component of the magnetic field, G
e	=	fundamental electronic charge, C
I_{TS}	=	current in the transverse solenoid, A
n_{Beam}	=	ion beam density, cm^{-3}
V_{Beam}	=	ion beam potential, V
V_D	=	retarding field energy analyzer discriminator voltage, V
V_{Local}	=	downstream local ion potential, V
V_p	=	plasma potential, V
x	=	*X* axial position, cm
x_{BC}	=	position of ion beam profile center, cm
x_{off}	=	*X* offset distance of ion beam vector from *z*-axis, cm
y	=	*Y* axial position, cm
z	=	*Z* axial position, cm
z_{DL}	=	*Z* axial position of the double-layer, cm
z_{RFEA}	=	*Z* axial position of the retarding field energy analyzer, cm
θ_{2P}	=	two-point steering angle between ion beam and *z*-axis, degrees
θ_{Beam}	=	angle between ion beam vector and *z*-axis, degrees
θ_{def}	=	angle of deflection of ion beam vector from the default ($I_{TS} = 0$ A) beam angle θ_{Beam}, degrees
σ_{0A}	=	standard deviation of the two-point steering angle at $z = 36$ cm for $I_{TS} = 0$ A, degrees
ϕ_{DL}	=	double-layer potential drop, V

Received 4 February 2010; revision received 13 April 2010; accepted for publication 14 April 2010.

*Ph.D. Candidate, Space Plasma, Power and Propulsion Group, Research School of Physics and Engineering; wes.cox@anu.edu.au. Student Member AIAA.

†Associate Professor, Space Plasma, Power and Propulsion Group, Research School of Physics and Engineering.

‡Professor, Space Plasma, Power and Propulsion Group, Research School of Physics and Engineering.

§Chief Technical Officer, 6 rue Laurent Pichat.

¶Innovation Manager, 6 rue Laurent Pichat.

I. Introduction

ELECTRIC propulsion (EP) technology has been developing over recent decades, with numerous EP systems, such as the gridded-ion thruster (GIT) and the Hall effect thruster (HET) [1,2], providing high specific impulse values (∼3000 s for the NSTAR GIT [3]). EP systems are suitable for both deep space missions and attitude control for spacecraft in geosynchronous Earth orbit. A number of successful deep space missions have flown with EP systems providing the primary in-space propulsion including the GIT propelled Deep Space-1 mission [3,4] and the HET propelled SMART-1 mission [5,6].

It is often beneficial to provide thrust offset from the spacecraft center of mass [7]. Providing deflection to the thrust vector can be achieved via a number of methods. Mechanical gimbals are the most common approach, which involves mounting the thruster on a structure that allows the physical tilting of the thruster attached to the spacecraft body [8,9]. Another option is influencing the ion beam after it has been accelerated by the thruster. This can be achieved by using solenoids or electrostatic plates to apply electromagnetic body forces to the charged particles in the beam [7,10]. The acceleration mechanism can also be perturbed which results in generation of the ion beam at an angle to the thruster axis. This can be executed by translating the acceleration grid in a GIT or offsetting the density distribution in a HET [7,11,12]. Finally, mounting multiple thrusters on the spacecraft body allows variable thrust levels from each which controls the overall thrust vector orientation [13].

Modifying the typically azimuthally symmetric magnetic field in EP systems has been simulated for a HET system [14] and investigated experimentally for the helicon double-layer thruster (HDLT) [15]. The HDLT is an electrodeless, neutralizer-free magnetoplasma thruster that has been demonstrated to accelerate ions in the potential drop of an electric double-layer (DL) experimentally [16–20],

theoretically [21–23] and through simulations [24,25]. The HDLT can be scaled in size and power [26,27] and has been demonstrated to operate with a variety of propellants [28,29]. Studies of the ion beam have identified a very low beam divergence (less than 10 deg for argon and 6 deg for xenon), with a constant exhaust velocity across the thruster radius [30,31]. Introduction of a transverse magnetic field (TMF) to the HDLT adds transverse components to the divergent magnetic field and this has been shown to produce asymmetry in the ion beam profile measured downstream of the DL [15].

In this work, an experimental, two-dimensional spatial mapping of the ion beam downstream of the DL under the influence of a TMF is performed in order to correlate the previously measured ion beam profile asymmetries to a deflected ion beam vector (IBV). Identification of IBV deflection under both polarities of the TMF is likely to suggest single-axis steering capability for the HDLT under the influence of a single transverse solenoid (TS). Operating a magnetically-steerable HDLT with a single TS incorporates the benefit of reduced complexity by avoiding mechanical gimbals and minimizing the additional solenoidal weight.

II. Experimental Setup and Diagnostics

The investigation into the effects of TMFs on the HDLT is performed in the Chi Kung experiment, the plasma reactor in which the DL generated ion beam was first detected [16] and on which the HDLT prototypes are based [30,32]. Chi Kung, as described previously [33] and shown in Fig. 1, consists of a 31 cm long, 15 cm-diam cylindrical Pyrex source tube attached contiguously to a 30 cm long, 32 cm-diam aluminum diffusion chamber. Surrounding the source tube (∼5 cm off the Pyrex surface) between $z = 3$ and 20 cm is a 1.5 mm thick, silver-coated, copper double-saddle helicon antenna (not shown in Fig. 1 for clarity) which is supplied with 250 W radio frequency power at 13.56 MHz via a manual, custom built L-matching network/generator system. The matching network consists of two tuneable capacitors: a 20–2000 pF load capacitor in parallel with the antenna and a 20–500 pF tune capacitor in series with the antenna. Surrounding the source tube, about 1 cm away from the antenna, are the primary solenoids. The primary solenoids consist of two coaxial solenoids placed at $(x, z) = (0, 1.4)$ cm (referred to as the source solenoid) and $(0, 21.1)$ cm (referred to as the exit solenoid) with their polarities both pointing north into the diffusion chamber (positive z-direction). The resulting magnetic field B_z exhibits a double-peak in the source tube along the z-axis with a maximum of ∼140 G extending into a diverging magnetic field of a few tens of gauss downstream in the diffusion chamber. The simulated magnetic field lines are shown as solid black lines in Fig. 1. Three-dimensional simulations of the magnetic field are performed using numerical integration of the Biot-Savart law. To determine the accuracy of the simulations, the z-component of the magnetic field along the z-axis is compared with gaussmeter measurements along the z-axis. The simulated and measured magnetic fields agree to within 6%.

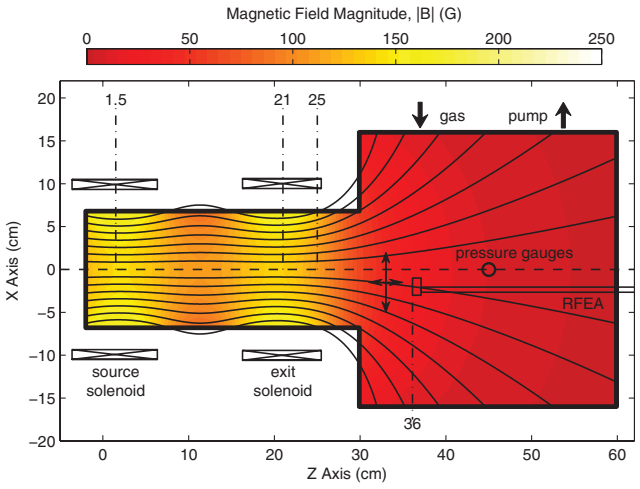

Fig. 1 Schematic of the Chi Kung plasma reactor.

The diffusion chamber is pumped down to a base pressure of 1.1×10^{-3} Pa (measured with an ion gauge positioned at the top of the diffusion chamber, at $(x, y, z) = (0, 16, 45)$ cm) using a 150 L/s turbomolecular/rotary pumping system attached to the side port in the diffusion chamber wall at $(x, y, z) = (16, 0, 54)$ cm. Argon gas is injected at a rate of 0.038 mg.s^{-1} via a chamber side port at $(x, y, z) = (16, 0, 37)$ cm and an operating pressure of 0.04 Pa is measured with a baratron gauge at the bottom of the diffusion chamber at $(x, y, z) = (0, -16, 45)$ cm. Measurements in an argon plasma operating at 250 W, 140 G and 0.04 Pa have observed a DL at $z_{DL} = 25$ cm (shown as a dashed-dotted line in Fig. 1, near the source tube exit) [34]. The interface between the source tube and diffusion chamber is defined as $z = 30$ cm, where the z-axis is along the primary axis of the cylindrical reactor. Inserted into the backplate of the diffusion chamber is a retarding field energy analyzer (RFEA) [35,36], as shown in Fig. 1. The probe is mounted on a slide and can be swept across the diameter of the backplate along the x-axis in the region between $x = -14$ and 14 cm and inserted/retracted along the z-axis, allowing the two-dimensional x-z plane to be investigated. Measurements in this plane can be performed without the need to break the vacuum to reposition the probe nor requiring approximations of cylindrical symmetry, as previously required [31].

To deflect the IBV to provide thrust at an angle to the primary axis (z-axis) of the HDLT, a TMF is applied via a single TS positioned at $(x, z) = (-16.2, 10.5)$ cm and aligned along the x-axis. The 10 cm long, 20 cm-inner-diam TS is similar to the primary solenoids with ∼800 turns of copper wire. Supplying the TS with a current of 3 A results in a maximum magnetic field magnitude $|B|$ of 123 G at the center of TS, while an effective current of 3 A in the source and exit solenoids individually produces a maximum magnetic field magnitude $|B|$ of 132 and 118 G, respectively. The current in the primary solenoids is referred to as effective as a consequence of their characteristic double winding, which requires a current of 6 A to be supplied to produce a current of 3 A to flow through the solenoidal wires [37]. Throughout the experiments, the source and exit solenoids consistently experience an effective current of 3 A each, with the polarity of the magnetic field pointing north into the diffusion chamber in the positive z-direction. The current in the TS is swept from $I_{TS} = 0$ to 6 A to produce TMFs of either polarity [north-in (Nin) or north-out (Nout)] and at varying magnitudes (ranging from 0 to 246 G at the center of the TS). Because the TS does not surround the source tube like the primary solenoids, the magnetic field at the center of TS of 0 to 246 G corresponds to a magnetic field (B_x) of 0 to 56 G at $(x, z) = (0, 10.5)$ cm (at the z-axis). The combination of the primary magnetic field (predominantly aligned along the z-axis) and TMF (predominantly along the x-axis) is not simply the summation of the two. Consequently, the combination of the two magnetic fields in the source result primarily in a deflection of the overall magnetic field from the z-axis and slight changes to the magnetic field magnitude (∼15 G change along the z-axis from $I_{TS} = 0$ to 3 A Nout).

Introducing the TMF to the Chi Kung source deflects the primary magnetic field lines (shown in Fig. 1 in the absence of the TMF), and the magnitude and direction of this deflection is dictated by the current supplied to the TS. This increasing deflection of the magnetic field lines in Chi Kung causes the plasma coupling to change and the matching network must be adjusted slightly for each TS current I_{TS} increment. Consequently the supplied radio-frequency power varies from 250 W by ±2 W due to these matching network changes. No significant changes to the plasma are visible through the small windows in the Chi Kung reactor as a function of the TMF. It is assumed that the introduction of the TMF does not cause the position of the DL to shift from $z = 25$ cm. The simulated magnetic field lines passing through $x = (-5.5, -2.25, 0, 2.25, 5.5)$ cm at $z = 30$ cm under the influence of the TMF is shown in Fig. 2 for the two TS polarities: Nout and Nin. The magnetic field lines passing through x (-2.25, 2.25) cm at $z = 30$ cm are not shown in the source ($z \leq 30$ cm) for clarity. The current is swept in 2 A increments: $I_{TS} = 0$ A (solid line), 2 A (dashed line), 4 A (dashed-dotted line),

and 6 A (dotted line), for both Nout and Nin. As the current in TS is increased, the field lines in the source are deflected increasingly parallel to the direction of the TS polarity, while the field lines in the diffusion chamber are increasingly deflected antiparallel. However, closer inspection of the magnetic field in the diffusion chamber shows that the interface between parallel and antiparallel deflection occurs at around $z = 40$ cm, depending on the x-position. Consequently, RFEA measurements of the ion beam between $z = 31$ and 36 cm will be performed in a region where the magnetic field lines are deflected parallel to the polarity of the TS. Over the $31 \leq z \leq 36$ cm range, the magnetic field lines at $x = 0$ cm deflect under the influence of the TMF by no more than 2 and 4 deg from the primary solenoidal field for TS Nin and Nout, respectively. At the center ($x = 0$ cm) of the previously measured DL position [34] ($z_{\mathrm{DL}} = 25$ cm), the angle of deflection of the $I_{\mathrm{TS}} > 0$ A magnetic field from the primary $I_{\mathrm{TS}} = 0$ A magnetic field for TS Nin and Nout is less than 7 and 11 deg, respectively.

Inserting the RFEA into the diffusion chamber, facing the plasma source (negative z-direction), and sweeping the RFEA discriminator voltage from $V_D = 0$ to 80 V in 0.4 V steps allows ions to be collected through the 2 mm-diam orifice as a function of their energy. Differentiating the collected ion current with respect to V_D enables the ion energy distribution function (IEDF) to be determined [38]. Measurements are not of the actual IEDF, but rather the energy of ions falling through the plasma sheath in front of the grounded RFEA [34]. When an ion beam is present, two populations of ions can be identified in the IEDF: a lower-energy local plasma population (denoted as *Local*) and a higher-energy ion beam population (denoted as *Beam*) [16]. The energy (eV_D) at the center of each of the two Gaussian profiles is regarded as the energy of each population. The difference between the two population energies is defined as the DL potential energy $e\phi_{\mathrm{DL}} = eV_{\mathrm{Beam}} - eV_{\mathrm{Local}}$. The ion beam density n_{Beam} is calculated to be the current measured by the RFEA at the beam potential V_{Beam} scaled by a simple calibration using a Langmuir probe biased at -70 V. In the absence of TMFs, the ion density just downstream of the previously measured [34] DL position ($z_{\mathrm{DL}} =$ 25 cm) is $\sim 5 \times 10^9$ cm^{-3} and decays exponentially with distance due to ion-neutral collisions [39]. The accuracy of the density measurements has been previously determined to be about $\pm 20\%$ due to calibration of the ion density from the total ion current measured with the RFEA [39].

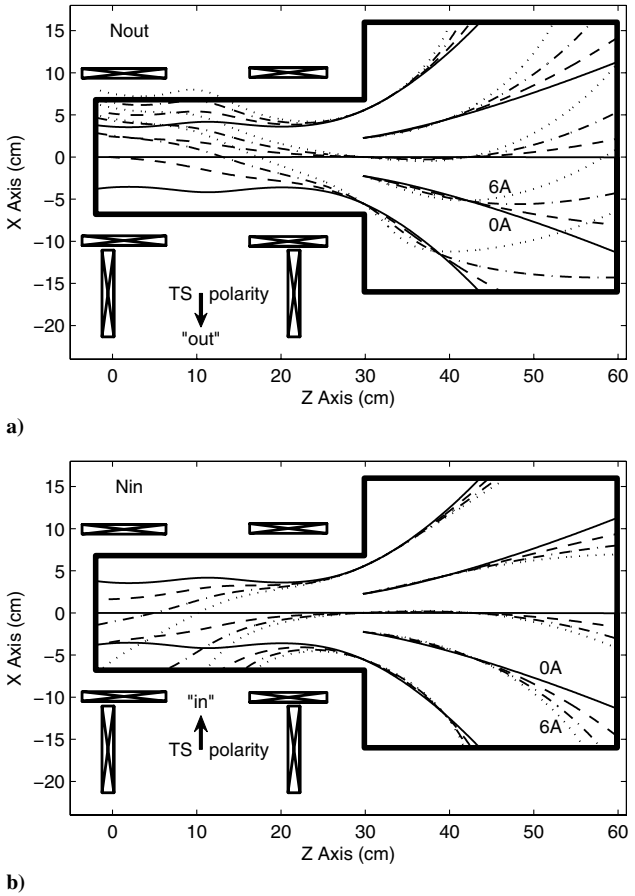

Fig. 2 The simulated magnetic field under the influence of the TMF of polarity a) Nout and b) Nin.

Previous RFEA measurements have demonstrated perturbation of the ion beam current profile (not calibrated to density) downstream of the DL (measured across the x-axis) under the influence of a Nout TMF [15]. In the present study, deflection of the IBV under the influence of a TMF (of both polarities) is investigated using two methods. Firstly, the ion beam deflection is investigated as a function of the TS current $0 \leq I_{\mathrm{TS}} \leq 6$ A to identify the solenoidal current regions likely to produce IBV deflection. Secondly, to measure the influence of the TMFs identified in the first method on the IBVs and subsequently identify the IBV alignment, the two-dimensional x-z plane is mapped out in the region $-14 \leq x \leq 14$ cm, $31 \leq z \leq 36$ cm.

III. Influence of the TS Current

Measurements of the ion beam density profile n_{Beam} at $z = 36$ cm (11 cm from the previously measured [34] DL position at $z_{\mathrm{DL}} =$ 25 cm) can be used to determine the influence on the ion beam of a TMF of increasing magnitude. The RFEA is swept in 1 cm intervals across the x-axis between $x = -14$ and 14 cm with measurements made for each TS current value from $I_{\mathrm{TS}} = 0$ to 6 A at increments of 1 A for both polarities. The ion beam density profile n_{Beam} for each value of I_{TS} is measured and the results are plotted as a color contour in Fig. 3. In agreement with previous measurements of the ion beam current profiles for TS Nout [15], the ion beam density profiles in Fig. 3 exhibit asymmetry as the current in the TS is increased, and this asymmetry is accompanied by an increase in the ion beam density n_{Beam} magnitude. The observed ion beam asymmetry measured at $z = 36$ cm is suggestive of a deflected ion beam, however, it is also possible that the ion beam may not be deflected at an angle but instead offset some distance x_{off} parallel to the z-axis.

An offset ion beam could be used to produce torque on the spacecraft body, however, for most spacecraft geometries the torsional effect of an offset ion beam will be diminished when compared with a deflected IBV. The RFEA measurements in this section focus on identifying asymmetries in the ion beam density n_{Beam} profile across the x-axis at $z = 36$ cm as a function of the current and polarity of the TS, similar to previous work [15]. The identified asymmetric ion beam density n_{Beam} profiles will subsequently be investigated spatially in the following section to determine if the IBV is deflected at an angle or if the ion beam is offset a distance x_{off} parallel to the z-axis. If the ion beam density n_{Beam} profiles across the x-axis measured at various z-positions are found to shift increasingly along the x-axis as the RFEA z-position is increased, deflection of the IBV will be observed. Alternatively, if the ion beam density n_{Beam} profiles across the x-axis remain unaffected by movement of the RFEA along the z-axis under the influence of the TMF, then the ion beam will be observed to be offset by a distance x_{off} parallel to the z-axis.

The circles in Fig. 3 (fit with quadratic solid black lines) denote the position of the center of the ion beam profiles, referred to as the beam center x_{BC}. The beam center positions x_{BC} are calculated using a method previously described [15]. Briefly, the ion beam profile is integrated between the two points intersecting with the full-width half maximum (FWHM) of the profile, referred to as the FWHM points. With this total integral calculated, the profile is cumulatively integrated from one FWHM point towards the other until the cumulative integral equals half the total integral. This point is defined as the beam center position x_{BC}. Using the beam center positions, an estimate of the beam angle can be obtained and the right vertical axis in Fig. 3 shows the inferred two-point steering angles θ_{2P}, scaled to coincide with the x-axis, calculated from the beam center positions x_{BC}. The dotted lines in Fig. 3 show the x-position and two-point steering angle θ_{2P} for the peak ion beam displacements at $I_{\mathrm{TS}} = 0$ to

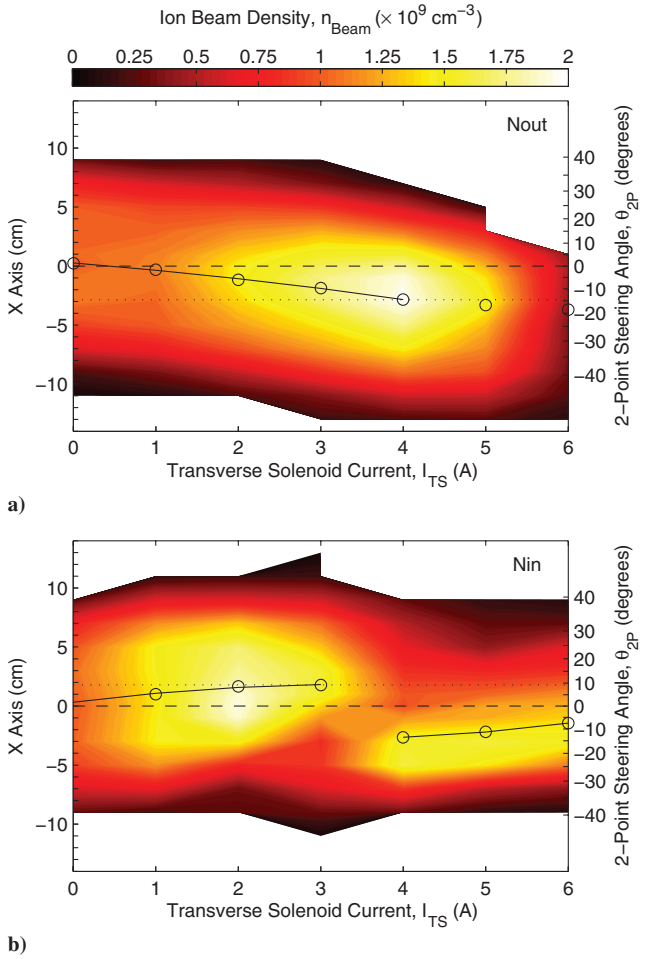

Fig. 3 The ion beam density n_{Beam} profiles measured across the x-axis at $z = 36$ cm with the TS polarized: a) Nout and b) Nin.

4 A Nout and 3 A Nin. The two-point steering angle θ_{2P} is calculated assuming the x-axially symmetric ion beam travels on a straight path from the center ($x = 0$ cm) of the DL position ($z_{DL} = 25$ cm) to the RFEA at $z_{RFEA} = 36$ cm such that

$$\theta_{2P} = \tan^{-1} \frac{x_{BC}}{z_{RFEA} - z_{DL}} \tag{1}$$

This calculation assumes the DL z-position is unchanged in the presence of the TMF. The spatial measurements of the ion beam in Sec. IV will evaluate the validity of the two-point steering angle by directly measuring the IBV under the influence of the TMF.

Figure 3a shows that for the Nout case both the ion beam density n_{Beam} and beam center position x_{BC} increase with I_{TS} until $I_{TS} = 4$ A. Beyond $I_{TS} = 4$ A, the ion beam density at x_{BC} decreases and the rate of beam center displacement decreases. The results for reversing the polarity to Nin are shown in Fig. 3b, which shows that n_{Beam} as a function of I_{TS} has a larger gradient than for the Nout case, and the x_{BC} positions are offset in the direction of the TS polarity up to a current of $I_{TS} = 3$ A for the Nin case. Beyond $I_{TS} = 3$ A, the Nin ion beam density profile suddenly jumps antiparallel to the TS polarity and then resumes shifting parallel to the TS polarity with increasing I_{TS}. Consequently, spatial measurements in Sec. IV with the RFEA in the region $-14 \leq x \leq 14$ and $31 \leq z \leq 36$ cm of the ion beam will be performed for TS currents up to $I_{TS} = 4$ A Nout and 3 A Nin.

As the current in the TS is swept from $I_{TS} = 0$ to 6 A in Fig. 3, the ion beam density at the beam center positions x_{BC} remain in the range $1 \times 10^9 \leq n_{Beam} \leq 2 \times 10^9$ cm^{-3} for both polarities. As discussed in Sec. II, source-facing RFEA measurements downstream of the DL reveal two ion populations with respective energies of eV_{Local} and eV_{Beam}. Measurements of the ion beam energy eV_{Beam} reflect the plasma potential energy eV_p just upstream of the DL [16]. Ions in the source region ($z < 30$ cm) at an energy eV_p passing through the DL at $z_{DL} = 25$ cm will be accelerated by the electric field of the DL into the diffusion chamber. As the current in the TS is increased (and thus the TMF magnitude) from $I_{TS} = 0$ to 6 A, the beam potential V_{Beam} remains relatively unchanged (within 10%) from ~55 V and the DL potential drop ϕ_{DL} decreases from ~20 V to about 10 V, for both polarities. Spatial RFEA measurements of the IBV should reveal whether the observed offset in the ion beam density profiles in Fig. 3 is the result of ion beam deflection or an ion beam offset from and parallel to the z-axis. A deflected ion beam will suggest that the plane of the DL has become tilted, such that ions accelerated in the electric field of the DL are accelerated at a pitch angle to the z-axis. The stable ion beam and DL potential measurements suggest that the magnitude of the accelerating potential structure inside Chi Kung remains relatively unaffected by the introduction of the TMF.

IV. Spatial Ion Beam Measurements

Spatial measurements of the ion beam density n_{Beam} are performed in the absence of the TMF (i.e. $I_{TS} = 0$ A) to obtain a baseline measurement to compare with measurements made in the presence of the TMF. The source-facing RFEA is swept across the x-axis in 1 cm x- and z-intervals, taking measurements in the region $-14 \leq x \leq 14$ cm and $31 \leq z \leq 36$ cm. The region is shown in Fig. 4a as the dashed box. A color contour plot of the n_{Beam} values measured with the RFEA is shown in Fig. 4b. The color contour in Fig. 4b shows the density measured by the RFEA, ranging from 0 to 2×10^9 cm^{-3}. These values will be used to obtain a relative comparison with the measurements of n_{Beam} for various TS current I_{TS} configurations to follow.

The circles in Fig. 4b indicate the calculated beam center positions x_{BC} for each sweep of the probe across the x-axis. The x_{BC} positions are fitted with a linear line of best fit (solid line) and the solid line through the x_{BC} positions is considered the IBV. In Fig. 4b, the angle between the IBV (solid line) and the z-axis (dashed line) is shown and is the beam angle, $\theta_{Beam}(0A) = 5.7$ deg. To evaluate the effect of the TMF on the ion beam, the difference between the $I_{TS} = 0$ A beam angle and the beam angles for $I_{TS} > 0$ A will be compared.

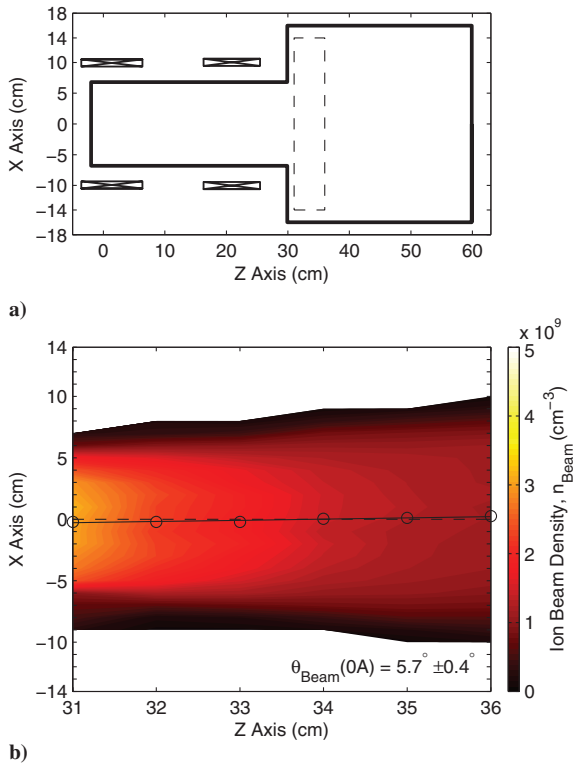

Fig. 4 a) Measurement region in Chi Kung for $I_{TS} = 0$ A and b) spatial ion beam density n_{Beam} measurements inside the measurement region.

Sweeping the discriminator voltage in 0.4 V increments from $V_D = 0$ to 80 V to measure the collected ion current as a function of V_D introduces an uncertainty of ± 0.4 V to the voltage at which the current is collected. Using this voltage uncertainty, the uncertainty in the angle of the IBV to the z-axis (θ_{Beam}) can be calculated as follows. Adding and subtracting 0.4 V to the obtained beam potential V_{Beam} results in what is defined as an upper and lower ion beam density n_{Beam}, respectively. Because a lower beam potential V_{Beam} corresponds to a greater number of ions collected, the upper and lower beam potentials measure smaller and greater ion beam densities, respectively. Calculating the upper and lower ion beam densities across each x-sweep of the RFEA in the range $-14 \leq x \leq 14$ cm, $31 \leq z \leq 36$ cm produces ion beam density n_{Beam} profiles that are smaller and greater (by up to 8% for $I_{\text{TS}} = 0$ A) in magnitude, respectively, but do not vary much in terms of asymmetry. Consequently, calculating the upper and lower beam center positions x_{BC} and the associated IBVs reveals a very small angular error as a result of the 0.4 V discriminator voltage V_D discretization. Uncertainties in the beam center positions are sufficiently small their error bars are indiscernible and have not been plotted in Fig. 4b. In the absence of TMFs, the uncertainty in the beam angle $\theta_{\text{Beam}}(0A) = 5.7$ deg is ± 0.4 deg. It is possible that there are other effects influencing the measurement, however, this calculation shows that uncertainty in the beam potential V_{Beam} generally causes an overall increase or decrease in the ion beam density n_{Beam} profile and has only a small effect on the resulting beam angle θ_{Beam}.

The observed $\theta_{\text{Beam}}(0A) = 5.7 \pm 0.4$ deg natural steer for $I_{\text{TS}} = 0$ A shown in Fig. 4b suggests that, in the absence of an applied asymmetry via a TMF, the ion beam exhibits a violation of cylindrical symmetry. The cylindrical geometry of the Chi Kung experiment should produce a plasma that exhibits azimuthal symmetry. Misalignment of the primary solenoids (source and exit) could lead to an angular uncertainty of the primary magnetic field of ~ 1 deg relative to the diffusion chamber, with the source tube angular uncertainty also ~ 1 deg relative to the diffusion chamber. These are insufficient to account for the natural steer observed in Fig. 4b. The measurements in Fig. 4b are the first spatial measurement of the ion beam in Chi Kung and show that ion beam symmetry is not produced. A possible explanation for this ion beam density asymmetry is the double-saddle antenna asymmetry [40], however, the focus of this study is the change to the ion beam in Fig. 4b under the influence of a TMF, not the properties of the ion beam in the baseline measurement itself.

A Nout TMF is generated by applying a current to the TS from $I_{\text{TS}} = 1$ to 4 A. Measurements of the ion beam density n_{Beam} under the influence of these Nout TMFs are performed by sweeping the source-facing RFEA across the x-axis in 1 cm x- and z-intervals, with measurements made in the region $-14 \leq x \leq 14$ cm and $31 \leq z \leq 36$ cm, as shown in Fig. 5a. The result of these n_{Beam} measurements are plotted as a color contour in Fig. 5b–5e. The beam center positions x_{BC} (circles) are calculated for each sweep of the RFEA across the x-axis and show a linear trend. Fitting the x_{BC} positions with a straight line (solid line) provides an indicator of the IBV. The beam angles θ_{Beam} shown in Fig. 5b–5e are calculated between the IBV (solid line) and the z-axis (dashed line). Uncertainty in the Nout beam angles θ_{Beam} are calculated as a result of the 0.4 V uncertainty in the discriminator voltage V_D described above and found to be less than ± 0.7 deg. As the current in the TS I_{TS} is increased, the straight IBV becomes increasingly deflected and the

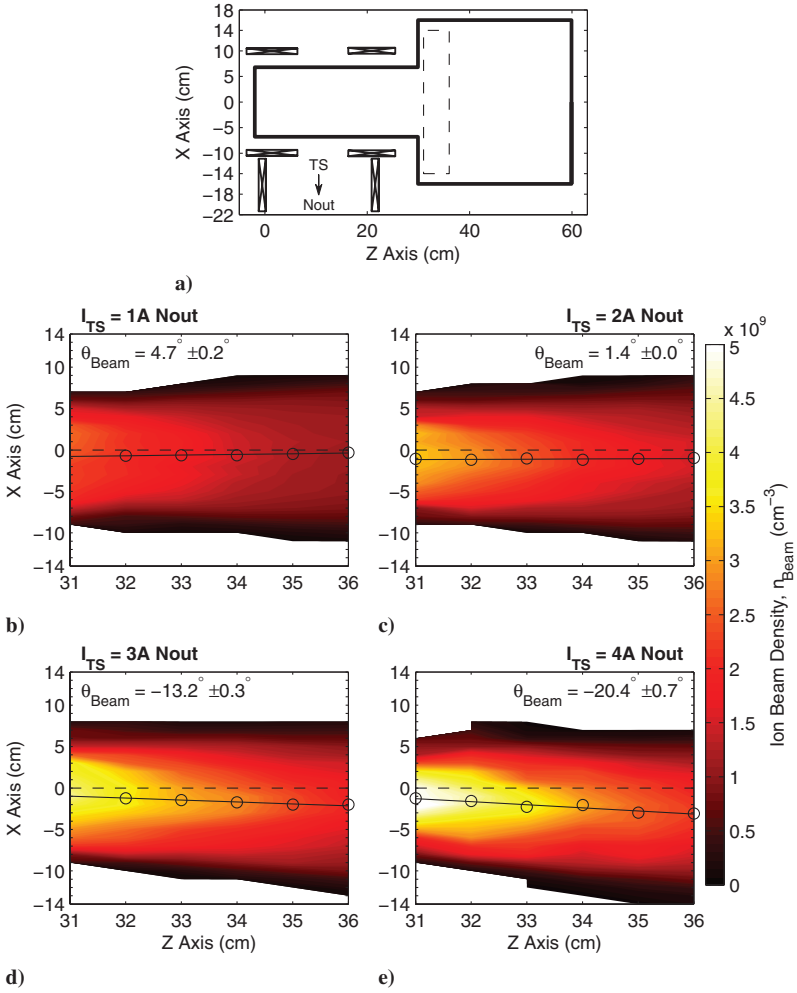

Fig. 5 a) Measurement region in Chi Kung and b–e) spatial ion beam density n_{Beam} measurements inside the measurement region for $I_{\text{TS}} = 1$–4 A Nout, respectively.

beam angle increases from the natural steer of $\theta_{\text{Beam}}(0A) = 5.7 \pm 0.4$ deg in the direction of the Nout TS polarity (in the negative x-direction). The observed IBV deflections suggest that the TMF induces a tilting of the plane of the DL, which results in ions that pass through the DL being accelerated at a pitch angle relative to the z-axis.

Spatial measurements of the ion beam under the influence of a Nin TMF are obtained by reversing the polarity of the TS. As before, the source-facing RFEA is swept across the x-axis in the region $31 \leq z \leq 36$ cm and $-14 \leq x \leq 14$ cm in increments of 1 cm in the x-z plane, as shown in Fig. 6a. As a consequence of the discontinuity in the behavior of the Nin ion beam density profile in Fig. 3b, I_{TS} is swept from 1 to 3 A in the current region identified in Sec. III as likely producing IBV deflection. The Nin spatial ion beam density measurements are shown as color contours in Fig. 6b–6d. The beam center positions x_{BC} (circles) show a linear trend which is fitted by a straight line (solid line), representing the IBV. Because of the discriminator voltage uncertainty of ± 0.4 V, the calculated uncertainty in the Nin beam angles θ_{Beam} is ± 0.5 deg. As the current in the TS I_{TS} is increased, the angle θ_{Beam} between the IBV (solid line) and the z-axis (dashed line) increases in the direction of the TS Nin polarity (in the positive x-direction).

Both the Nout and Nin measurements of the ion beam density n_{Beam} in Fig. 5 and 6, respectively, show straight IBVs which are deflected at an increasing angle as a function of the current I_{TS} in the TS. Therefore, the effect of the TMF is to deflect the ion beam at an angle, and not offset the ion beam a distance from and parallel to the z-axis. Calculating the difference between the natural steer angle of $\theta_{\text{Beam}}(0A) = 5.7 \pm 0.4$ deg and the TMF beam angle θ_{Beam} ($I_{\text{TS}} > 0$ A) produces the angle of deflection $\theta_{\text{def}} = \theta_{\text{Beam}}(0A) - \theta_{\text{Beam}}$: the angle through which the ion beam is deflected by the TMF. Figure 7 shows the values of θ_{def} (and the two-point steering angles θ_{2P} from Fig. 3), for both TS polarities. The values of θ_{def} and θ_{2P} for the TS Nout case are each multiplied by a factor of (-1) to compare the magnitudes of θ_{def} and θ_{2P} for both polarities. The $I_{\text{TS}} = 0$ A two-point steering angle offset of 1.8 ± 0.6 deg is removed from the values of θ_{2P} plotted in Fig. 7 to allow comparison with the deflection angles. The two-point steering angle error bars are calculated similarly to the deflection angle θ_{def} error bars, with the uncertainty in the beam center positions x_{BC} determined as a result of a ± 0.4 V uncertainty in the discriminator voltage V_D. Uncertainty in the two-point steering angle θ_{2P} is calculated using the upper and lower x_{BC} positions in Eq. (1). Figure 7 shows that the angles of deflection follow similar trends for both polarities and suggests that the mechanism behind Nout and Nin magnetic steering is similar. Maximum angles of deflection of up to $(-1)\theta_{\text{def}} = 26$ deg for TS Nout (at 4 A) and $\theta_{\text{def}} = 14$ deg TS Nin (at 3 A) are measured under the influence of the TMF.

Estimation of the effect of ion beam density n_{Beam} measurement uncertainty on the deflection angle θ_{def} using the discriminator voltage uncertainty of ± 0.4 V, described above, does not take into account all the effects which can cause uncertainty in the n_{Beam} measurements. To compensate for this, the standard deviation of the beam center position x_{BC} measured with eight individual sweeps of the RFEA across the x-axis at $z = 36$ cm for $I_{\text{TS}} = 0$ A can be calculated and plotted in Fig. 7. Performing repeated measurements of the ion beam density n_{Beam} across the x-axis for each z-position under each I_{TS} configuration is beyond the scope of the study. However by determining the standard deviation for the single case of $I_{\text{TS}} = 0$ A at $z = 36$ cm, we can evaluate the validity of the

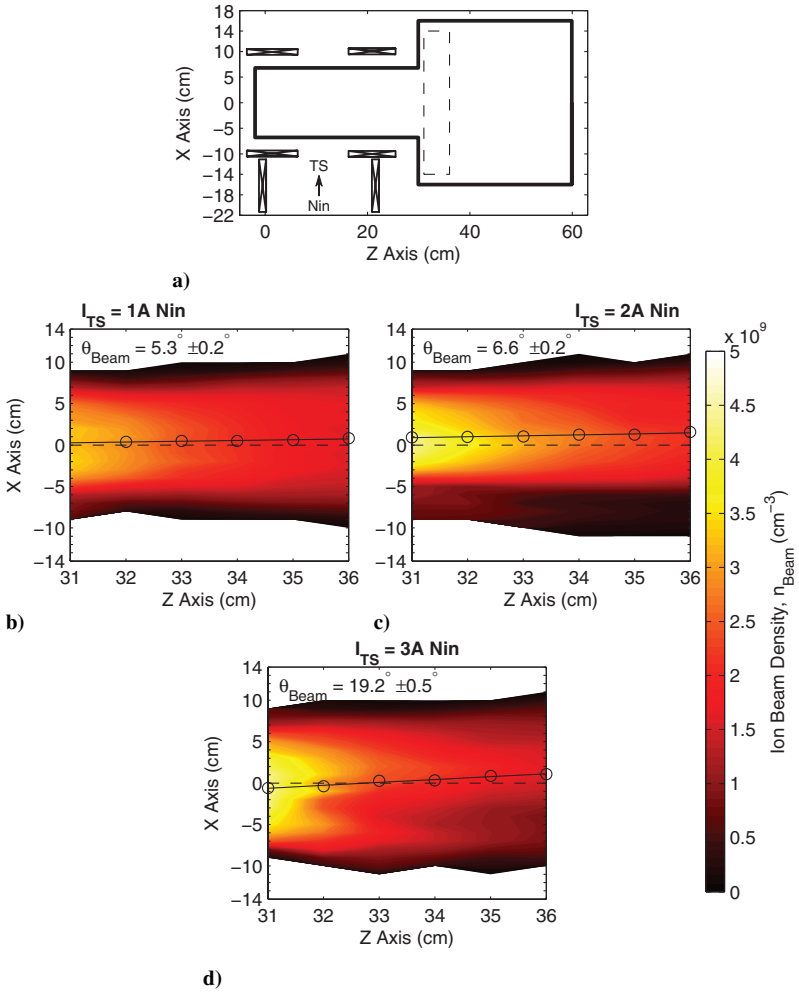

Fig. 6 a) Measurement region in Chi Kung and b–d) spatial ion beam density n_{Beam} measurements inside the measurement region for $I_{\text{TS}} = 1$–3 A Nin, respectively.

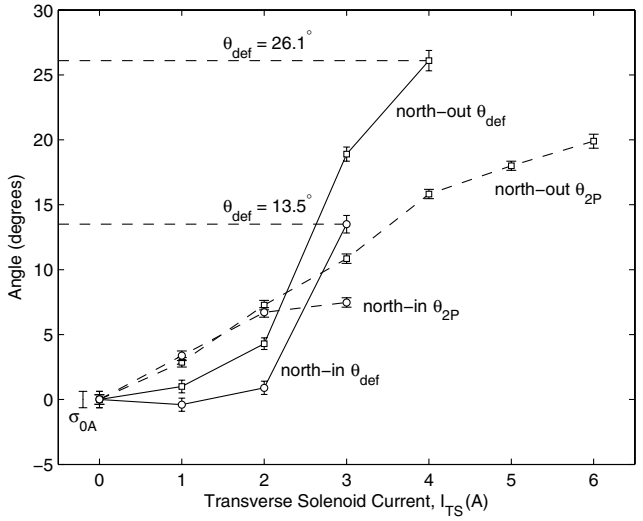

Fig. 7 Deflection angles $\theta_{\mathbf{def}}$ and two-point steering angles θ_{2P}.

discriminator voltage uncertainty analysis used to obtain the error bars plotted in Fig. 7 and show the scale of random noise in these measurements. The standard deviation in the beam center position x_{BC} at $z = 36$ cm for $I_{\mathrm{TS}} = 0$ A is calculated to be ± 0.1 cm, resulting in a two-point steering angle (calculated using Eq. (1)) with a standard deviation of $\sigma_{0A} = \pm 0.6$ deg. The θ_{2P} standard deviation σ_{0A} is plotted to the left of the $I_{\mathrm{TS}} = 0$ A angles in Fig. 7 and shows that the standard deviation measured at this point is similar to the uncertainty of both θ_{2P} and θ_{def} calculated as a result of the ± 0.4 V discriminator voltage V_D uncertainty.

The values of ion beam deflection obtained here (total single-axis range $\sim 40 \pm 1$ deg) are significant since gimbal steering systems usually operate within a maximum range of about ± 5 deg [12]. Simulations performed on a Hall thruster to investigate the potential use of a magnetic thrust vectoring system have demonstrated that the ion beam angular distributions may be varied in the range of 10 deg [14].

In this work it has been shown that the IBVs are deflected under the influence of the TMF of both polarities and the angles of deflection θ_{def} scale with increasing TS current I_{TS}. The deflection angle θ_{def} trend roughly follows the behavior inferred from the two-point steering angle θ_{2P} calculations, with both angles (θ_{def} and θ_{2P}) plotted in Fig. 7 for both TS polarities. The two-point steering angle provides a good first order approximation of the deflection angle, with values of θ_{def} and θ_{2P} differing by at most 80% for both the Nout case and the Nin case.

At a TS current of $I_{\mathrm{TS}} = 4$ A Nout and $I_{\mathrm{TS}} = 3$ A Nin, the magnetic field lines in the measurement region ($31 \leq z \leq 36$ cm) are all deflected from the $I_{\mathrm{TS}} = 0$ A field lines by less than 5 deg. At the position of the DL ($z_{\mathrm{DL}} = 25$ cm) the magnetic deflection is less than 8 deg. This magnetic field deflection is significantly less than that exhibited by the ion beam under the influence of the TMF (-26 and 14 deg for TS Nout and Nin, respectively). If the ions were following the field lines, the ion beam would be deflected at most by the angle of the field lines. The significant discrepancy between the angle of the magnetic field and the deflected ion beam suggests that the angle of the magnetic field under the influence of a TMF is not the dominant factor in controlling the angle of ion beam deflection. The straight, deflected IBVs in Fig. 5 and 6 suggest the TMF induces a tilt to the plane of the DL. Determining the complex interaction between the TMF and the DL (and the magnitude of the possible DL tilt) is well beyond the scope of this work and represents an avenue for future study.

V. Conclusions

The introduction of a TMF is found to deflect the ion beam generated by a helicon DL plasma, with the direction of the deflection determined by the polarity of the TMF and without any significant degradation to the DL and ion beam characteristics. Ion beam deflection angles of up to $(-1)\theta_{\mathrm{def}} = 26.1 \pm 0.8$ and $\theta_{\mathrm{def}} = 13.5 \pm 0.7$ deg are measured for TS currents of $I_{\mathrm{TS}} = 4$ A for the Nout case and $I_{\mathrm{TS}} = 3$ A for the Nin case, respectively. The ion beam density n_{Beam} is observed to remain in the range $1 \times 10^9 \leq n_{\mathrm{Beam}} \leq 2 \times 10^9$ cm^{-3} at the center of the ion beam profiles x_{BC} as the current in the TS is swept from $I_{\mathrm{TS}} = 0$ to 6 A for both polarities. It is proposed that the TMF induces a tilt to the DL, causing ions to be accelerated at a pitch angle to the z-axis.

In terms of its application, introducing a TS to the HDLT provides an experimental demonstration of magnetically-induced thrust vectoring of an EP system. By demonstrating thrust vectoring in two directions (positive and negative x-direction) using only a single solenoid, it is possible to provide thrust vectoring without the additional dry mass of a second TS. Magnetic thrust vectoring may provide an alternative for missions where a mechanical gimbal structure or multiple thrusters are inappropriate due to the reduced complexity and wide angular range.

Acknowledgments

This work is conducted under innovation funding from ASTRIUM CTO and funding from the Australian Research Council Linkage grant LP 0883456 in collaboration with EADS-ASTRIUM. The authors wish to thank P. Alexander for his technical assistance on this project and R. Hawkins for his assistance with magnetic field simulation.

References

[1] Jahn, R. G., and Choueiri, E. Y., *Encyclopedia of Physical Science and Technology, Electric Propulsion*, Vol. 5, 3rd ed., Academic Press, New York, 2002, pp. 125–141.

[2] Martinez-Sanchez, M., and Pollard, J. E., "Spacecraft Electric Propulsion: An Overview," *Journal of Propulsion and Power*, Vol. 14, No. 5, 1998, pp. 688–699. doi:10.2514/2.5331

[3] Brophy, J. R., "NASA's Deep Space 1 Ion Engine (Plenary)," *Review of Scientific Instruments*, Vol. 73, No. 2, 2002, pp. 1071–1078. doi:10.1063/1.1432470

[4] Brophy, J. R., and Noca, M., "Electric Propulsion for Solar System Exploration," *Journal of Propulsion and Power*, Vol. 14, No. 5, 1998, pp. 700–707. doi:10.2514/2.5332

[5] Kugelberg, J., Bodin, P., Persson, S., and Rathsman, P., "Accommodating Electric Propulsion on SMART-1," *Acta Astronautica*, Vol. 55, No. 2, 2004, pp. 121–130. doi:10.1016/j.actaastro.2004.04.003

[6] Racca, G. D., Marini, A., Stagnaro, L., van Dooren, J., di Napoli, L., Foing, B. H., Lumb, R., Volp, J., Brinkmann, J., Grünagel, R., Estublier, D., Tremolizzo, E., McKay, M., Camino, O., Schoemaekers, J., Hechler, M., Khan, M., Rathsman, P., Andersson, G., Anflo, K., Berge, S., Bodin, P., Edfors, A., Hussain, A., Kugelberg, J., Larsson, N., Ljung, B., Meijer, L., Mörtsell, A., Nordebäck, T., Persson, S., and Sjöberg, F., "SMART-1 Mission Description and Development Status," *Planetary and Space Science*, Vol. 50, Nos. 14–15, 2002, pp. 1323–1337. doi:10.1016/S0032-0633(02)00123-X

[7] Fearn, D. G., "Ion Thruster Thrust Vectoring Requirements and Techniques," 27th International Electric Propulsion Conference, Pasadena, CA, 15–19 Oct. 2001.

[8] Vaughan, D. A., "Gimbal Development for the NEXT Ion Propulsion System," 41st AIAA/ASME/SAE/ASEE Joint Propulsion Conference and Exhibit, Tuscon, AZ, 10–13 July 2005.

[9] Brophy, J. R., Anderson, J. R., Benson, G., Bond, T., Brinza, D., Bushway, D., Cardwell, H., Christensen, J., Fujii, K. K., Gallagher, J., Kakuda, R. Y., Hamley, J., Henry, M. D., Mantha, K. R., Marcucci, M. G., Matranga, M., Patterson, M., Polk, J. E., Rawlin, V., Sovey, J., and Stocky, J. F., "Ion Propulsion System (NSTAR)," Jet Propulsion Lab., Deep Space 1 Technology Validation Reports, JPL Publication 00-10, Pasadena, CA, Oct. 2000.

[10] Vieira, I., Gargaté, L., and Mendonça, J. T., "Convergence and Deflection of a Hall Thruster Plume," 28th International Electric Propulsion Conference, Toulouse, France, 2003.

[11] Jameson, P., "Thrust Steering of a Gridded Ion Engine," Fourth International Spacecraft Propulsion Conference, Cagliari, Sardinia, Italy, 2–4 June 2004.

[12] Kural, A., Leveque, N., Welch, C., and Wolanski, P., "Design of an Ion Thruster Movable Grid Thrust Vectoring System," *Acta Astronautica*, Vol. 55, Nos. 3–9, 2004, pp. 421–432. doi:10.1016/j.actaastro.2004.05.037

[13] Duchemin, O., Lorand, A., Notarianni, M., and Valentian, D., "Multi-Channel Hall-Effect Thrusters: Mission Applications and Architecture Trade-Offs," 30th International Electric Propulsion Conference, Florence, Italy, 17–20 Sept. 2007.

[14] Garrigues, L., Boniface, C., Hagelaar, G. J. M., Boeuf, J. P., and Duchemin, O., "Performance Modeling of a Thrust Vectoring Device for Hall Effect Thrusters," *Journal of Propulsion and Power*, Vol. 25, No. 5, 2009, pp. 1003–1012. doi:10.2514/1.39680

[15] Charles, C., Boswell, R. W., Cox, W., Laine, R., and MacLellan, P., "Magnetic Steering of a Helicon Double Layer Thruster," *Applied Physics Letters*, Vol. 93, No. 20, 2008, pp. 201501–201503. doi:10.1063/1.3033201

[16] Charles, C., and Boswell, R. W., "Laboratory Evidence of a Supersonic Ion Beam Generated by a Current-Free 'Helicon' Double-Layer," *Physics of Plasmas*, Vol. 11, No. 4, 2004, pp. 1706–1714. doi:10.1063/1.1652058

[17] Takahashi, K., Oguni, K., Yamada, H., and Fujiwara, T., "Ion Acceleration in a Solenoid-Free Plasma Expanded by Permanent Magnets," *Physics of Plasmas*, Vol. 15, No. 8, 2008, pp. 084501–084504. doi:10.1063/1.2965497

[18] Charles, C., "A Review of Recent Laboratory Double Layer Experiments," *Plasma Sources Science and Technology* , Vol. 16, No. 4, 2007, pp. R1–R25. doi:10.1088/0963-0252/16/4/R01

[19] Cohen, S. A., Siefert, N. S., Stange, S., Boivin, R. F., Scime, E. E., and Levinton, F. M., "Ion Acceleration in Plasmas Emerging from a Helicon-Heated Magnetic-Mirror Device," *Physics of Plasmas*, Vol. 10, No. 6, 2003, pp. 2593–2598. doi:10.1063/1.1568342

[20] Sun, X., Biloiu, C., Hardin, R., and Scime, E. E., "Parallel Velocity and Temperature of Argon Ions in an Expanding, Helicon Source Driven Plasma," *Plasma Sources Science and Technology* , Vol. 13, No. 3, 2004, pp. 359–370. doi:10.1088/0963-0252/13/3/001

[21] Lieberman, M. A., and Charles, C., "Theory for Formation of a Low-Pressure, Current-Free Double Layer," *Physical Review Letters*, Vol. 97, No. 4, 2006, pp. 045003–045006. doi:10.1103/PhysRevLett.97.045003

[22] Fruchtman, A., "Electric Field in a Double Layer and the Imparted Momentum," *Physical Review Letters*, Vol. 96, No. 6, 2006, pp. 065002–065005. doi:10.1103/PhysRevLett.96.045005

[23] Chen, F. F., "Physical Mechanism of Current-Free Double Layers," *Physics of Plasmas*, Vol. 13, No. 3, 2006, pp. 034502–034504. doi:10.1063/1.2179393

[24] Meige, A., Boswell, R. W., Charles, C., and Turner, M. M., "One-Dimensional Particle-in-Cell Simulation of a Current-Free Double Layer in an Expanding Plasma," *Physics of Plasmas*, Vol. 12, No. 5, 2005, pp. 052317–052326. doi:10.1063/1.1897390

[25] Gesto, F. N., Blackwell, B. D., Charles, C., and Boswell, R. W., "Ion Detachment in the Helicon Double-Layer Thruster Exhaust Beam," *Journal of Propulsion and Power*, Vol. 22, No. 1, 2006, pp. 24–30. doi:10.2514/1.13914

[26] Sutherland, O., Charles, C., Plihon, N., and Boswell, R. W., "Experimental Evidence of a Double Layer in a Large Volume Helicon Reactor," *Physical Review Letters*, Vol. 95, No. 20, 2005, pp. 205002–205005. doi:10.1103/PhysRevLett.95.205002

[27] Virko, V. F., Virko, Y. V., Slobodyan, V. M., and Shamrai, K. P., "The Effect of Magnetic Configuration on Ion Acceleration from a Compact Helicon Source with Permanent Magnets," *Plasma Sources Science and Technology* , Vol. 19, No. 1, 2010, pp. 015004–015010. doi:10.1088/0963-0252/19/1/015004

[28] Charles, C., Boswell, R. W., Laine, R., and MacLellan, P., "An Experimental Investigation of Alternative Propellants for the Helicon Double Layer Thruster," *Journal of Physics D: Applied Physics*, Vol. 41, No. 17, 2008, pp. 175213–175218. doi:10.1088/0022-3727/41/17/175213

[29] Charles, C., "Plasmas for Spacecraft Propulsion," *Journal of Physics D: Applied Physics*, Vol. 42, No. 16, 2009, pp. 163001–163018. doi:10.1088/0022-3727/42/16/163001

[30] Charles, C., Boswell, R. W., and Lieberman, M. A., "Xenon Ion Beam Characterization in a Helicon Double Layer Thruster," *Applied Physics Letters*, Vol. 89, No. 26, 2006, pp. 261503–261505. doi:10.1063/1.2426881

[31] Cox, W., Charles, C., Boswell, R. W., and Hawkins, R., "Spatial Retarding Field Energy Analyzer Measurements Downstream of a Helicon Double Layer Plasma," *Applied Physics Letters*, Vol. 93, No. 7, 2008, pp. 071505–071507. doi:10.1063/1.2965866

[32] West, M. D., Charles, C., and Boswell, R. W., "Testing a Helicon Double Layer Thruster Immersed in a Space-Simulation Chamber," *Journal of Propulsion and Power*, Vol. 24, No. 1, 2008, pp. 134–141. doi:10.2514/1.31414

[33] Charles, C., and Boswell, R. W., "Time Development of a Current-Free Double-Layer," *Physics of Plasmas*, Vol. 11, No. 8, 2004, pp. 3808–3812. doi:10.1063/1.1764829

[34] Charles, C., and Boswell, R., "Current-Free Double-Layer Formation in a High-Density Helicon Discharge," *Applied Physics Letters*, Vol. 82, No. 9, 2003, pp. 1356–1358. doi:10.1063/1.1557319

[35] Conway, G. D., Perry, A. J., and Boswell, R. W., "Evolution of Ion and Electron Energy Distributions in Pulsed Helicon Plasma Discharges," *Plasma Sources Science and Technology* , Vol. 7, No. 3, 1998, pp. 337–347. doi:10.1088/0963-0252/7/3/012

[36] Charles, C., Degeling, A. W., Sheridan, T. E., Harris, J. H., Lieberman, M. A., and Boswell, R. W., "Absolute Measurements and Modeling of Radio Frequency Electric Fields Using a Retarding Field Energy Analyzer," *Physics of Plasmas*, Vol. 7, No. 12, 2000, pp. 5232–5241. doi:10.1063/1.1322557

[37] Charles, C., "High Source Potential Upstream of a Current-Free Electric Double Layer," *Physics of Plasmas*, Vol. 12, No. 4, 2005, pp. 044508–044511. doi:10.1063/1.1883182

[38] Böhm, C., and Perrin, J., "Retarding-Field Analyzer for Measurements of Ion Energy Distributions and Secondary Electron Emission Coefficients in Low-Pressure Radio Frequency Discharges," *Review of Scientific Instruments*, Vol. 64, No. 1, 1993, pp. 010031–010044.

[39] Charles, C., "High Density Conics in a Magnetically Expanding Helicon Plasma," *Applied Physics Letters*, Vol. 96, No. 5, 2010, pp. 051502–051504. doi:10.1063/1.3309668

[40] Charles, C., Boswell, R. W., and Lieberman, M. A., "Energy Balance in a Low Pressure Capacitive Discharge Driven by a Double-Saddle Antenna," *Physics of Plasmas*, Vol. 10, No. 3, 2003, pp. 891–899. doi:10.1063/1.1555058

L. King
Associate Editor